CrossMark

Flow simulation and solidification phenomena of AC4CH aluminum alloy in semi-solid forging process by explicit MPS method

Amit Regmi[1] · Hiroki Shintaku[2] · Tsutomu Sasaki[3] · Seiichi Koshizuka[4]

Abstract Semi-solid forging (SSF) is a powerful manufacturing technology to fabricate near-net shaped products in automotive industries. During SSF process, the filling behavior and solidification process of AC4CH aluminum alloy is presented in this paper. The explicit MPS method program solving Navier–Stokes equation is coupled with heat transfer and solidification has been used to predict the filling pattern and temperature distribution of semi-solid material (SSM). The non-Newtonian rheological model was used as the constitutive equation of SSM. In this study, numerical analysis of SSF was carried out in box cavity with various flange thickness (4, 8, 12 and 16 mm) and corresponding experiments were undertaken for AC4CH aluminum alloy with solid fraction less than 0.5. The numerical results of SSM filling pattern and solidification phenomena in flange were validated with the experimental results. During solidification process, flow calculation was stopped and only thermal calculation was carried out. The shrinkage defect was well predicted near the lower mid area of the box cavity with flange thickness 16 mm.

✉ Amit Regmi
amitregmi11@gmail.com

1   E&T Co., Ltd., 2-17-1, Saiwai Cho,
    Kawaguchi Shi 332-0016, Japan

2   Yachiyo Industry Co., Ltd., 1959-5, Oshiage,
    Sakura Shi 329-1334, Japan

3   Goshi Giken Co., Ltd., 1280, Toyooka, Koshi Shi,
    Kumamoto Prefecture 861-1115, Japan

4   The University of Tokyo, 7-3-1, Hongo,
    Bunkyo-Ku 113-8656, Japan

1 Introduction

In recent years, aluminum alloy are widely used in various automotive and aerospace industries because of their properties like light weight, high strength and rigidity. From manufacturing perspective, SSF provides a substantial potential as an innovative net shape manufacturing process [1–7]. In 1971 Spencer et al. started studying the rheological properties of semi-solid alloy at MIT [8]. Since then, this process has become a widely studied and accepted as an effective net shape forging process at semi-solid state. Semi-solid materials (SSM) for SSF are generally produced by stirring molten metallic alloy at high angular velocity to form special microstructure during solidification. In this state the microstructure consists of solid metal spheroids in liquid matrix so-called thixotropic properties [9,10].

Due to the thixotropic behavior, SSM has stable viscous flow pattern in comparison to the conventional casting. This provides sound mechanical properties without defects such as porosity and air entrapment and inhomogeneous dendritic structure during solidification [11–13]. The main advantages of forging in semi-solid state are low forming temperature in comparison to the traditional casting and low forming load in comparison to the traditional forging [14–16]. Besides that, this process is also capable of fabricating complex shaped components in one process. But according to the complexity of die shapes and design there may be existence of solidification of the liquid phase which may cause shrinkage defects [17,18].

Various researchers have conducted the experimental and numerical investigation to understand the SSF process. Charreyron and Flemings [19] studied the compression behavior of Pb–Sn semi-solid alloy by the upper-bound method. Nguyen et al. [20] compared the theoretical and experimental study of the isothermal mechanical behavior of alloys in

the semi-solid state. Kang et al. [21] carried out the filling analysis of semi-solid aluminum alloy by SMAC method. Lee et al. [22] investigated the die filling and solidification phenomenon in semi-solid injection forging process using MAGMA software. Cleary et al. [23–25] studied the flow prediction and experimental validation in high pressure die casting process by using SPH method.

In this study, explicit MPS method was used for flow and solidification analysis of the SSF process of AC4CH aluminum alloy in the box cavity with various flange thickness of 4, 8, 12 and 16 mm. The non-Newtonian rheological model was adopted for the flow simulation of SSM. After complete filling, solidification analysis was conducted in box cavity with flange thickness 16 mm. In this study, solidification phenomena mean thermal calculation of box cavity without considering flow calculation. During this, temperature of the SSM decreases from 503 to 371°C in 10 s by conduction heat transfer from upper and lower dies. The numerical results filling pattern and solidification phenomena in flange are validated with an experiment result and the shrinkage defect was well predicted near the lower mid area of the flange.

2 MPS method

2.1 Governing equation

MPS method is a Lagrangian continuum method for solving systems of partial differential equations. In this study, fluid flow and heat transfer equations are coupled to simulate the flow behavior of a semi-solid material in the SSF process. The mass, momentum and energy conservation equations for incompressible flows are expressed as follow:

$$\frac{D\rho}{Dt} = 0 \tag{1}$$

$$\rho \frac{Du}{Dt} = -\nabla p + \mu \nabla^2 u + \rho g \tag{2}$$

$$C_p \rho \frac{DT}{Dt} = k \nabla^2 T + q \tag{3}$$

where ρ is the density, u is the velocity vector, P is the pressure, μ is the viscosity, and g is the body force vector including gravity, C_p is the fluid specific heat, k is the thermal conductivity, T is the temperature, and q is the source of heat generation or loss.

2.2 Discretization technique

In MPS method the governing equations are discretized by replacing the differential operators with the following gradient and laplacian approximations [26]:

$$\langle \nabla \phi \rangle_i^k = \frac{d}{n^0} \sum_{j \neq i} \frac{\left(\phi_j^k - \phi_i^k \right)}{\left| r_j^k - r_i^k \right|^2} \left(r_j^k - r_i^k \right) \omega(|r_j - r_i|) \tag{4}$$

$$\langle \nabla^2 \phi \rangle_i^k = \frac{2d}{\lambda n^0} \sum_{j \neq i} \left[\left(\phi_j^k - \phi_i^k \right) \omega(|r_j - r_i|) \right] \tag{5}$$

where d is the number of space dimensions, and n^0 is the initial particle number density which is fixed for incompressibility condition. Φ_i is the physical quantity of the i-th particle. The function ω is a weight function, which is given as follows:

$$\omega(r) = \begin{cases} \frac{r_e}{r} - 1 : (0 \leq r < r_e) \\ 0 : (r_e \leq r) \end{cases} \tag{6}$$

where r is the distance between two particles and r_e represents the effective range of particle interaction. The particle number density (n_i) is the summation of the weight of neighboring particles and is expressed as follows:

$$n_i = \sum_{j \neq i} \left[\omega \left(|r_j^- r_i| \right) \right] \tag{7}$$

where r_j and r_i are the position vectors of particles j and i respectively. The constant particle number density n^0 is proportional to the fluid density and must be constant to satisfy the mass conservation equation (Eq. 1). It is also interpreted as the normalization factor of the weighted average.

The parameter λ in Eq. 5 is a constant calculated as follows:

$$\lambda = \frac{\sum\limits_{j \neq i} |r_j - r_i|^2 \omega(|r_j - r_i|)}{\sum\limits_{j \neq i} \omega(|r_j - r_i|)} \tag{8}$$

This parameter adjusts the increase in the variance of the laplacian approximation to that of the analytical solution.

2.3 Explicit MPS algorithm

The flow chart of the explicit MPS method for the SSF process is as shown in Fig. 1. The numerical algorithm is mainly divided into four steps.

In the first step, thermal diffusion is calculated explicitly using Hirata and Anzai's discretization technique [27]. The temperature at the next time step $k + 1$ is obtained from the temperature distribution at the present time step k as follows.
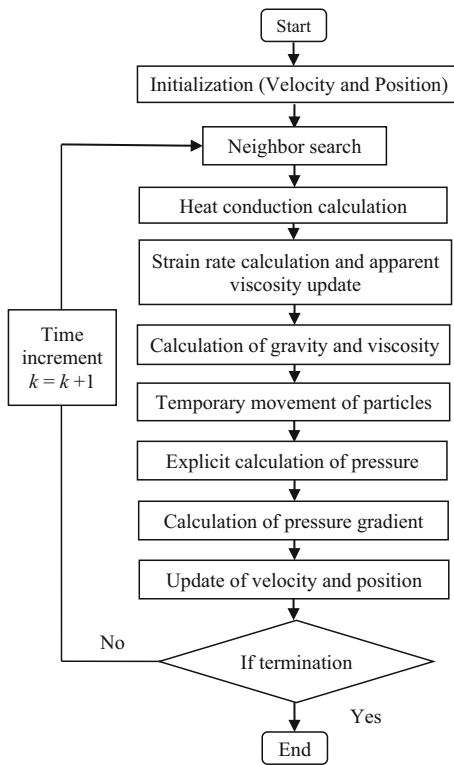
Fig. 1 Explicit MPS algorithm for SSF

$$\frac{T_i^{k+1} - T_i^k}{\Delta t}$$

$$= \frac{2d}{\rho C_p n^0} \sum_{j \neq i} \frac{\left(T_j^k - T_i^k\right)}{\left(\frac{1}{2\zeta_i} + \frac{1}{2\zeta_j} + \frac{R}{\left|r_i^k - r_j^k\right|}\right)} \frac{\omega(|r_j - r_i|)}{\left|r_i^k - r_j^k\right|^2} \quad (9)$$

where ζ is the thermal conductivity, T is the temperature and R is the heat resistance. T_i and T_j are the surface temperatures of materials i and j at the interface between the materials having thermal conductivity ζ_i and ζ_j. During wall and material thermal contact Eq. (9) is modified as $\zeta_j = \zeta_{wall}$.

Then, in the second step, the strain rate is calculated as:

$$\dot{\gamma} = \sqrt{2D:D} \quad (10)$$

$$D = \frac{1}{2}\left\{\langle\nabla U\rangle + \langle\nabla U^t\rangle\right\} \quad (11)$$

where γ is the shear rate and D is the deformation rate tensor. After the temperature and strain rate calculations, viscosity of each particle i is updated by considering the changes in temperature and strain rate.

In the third step, contributions of the body force and the viscosity dissipation are calculated:

$$\left\langle\nabla^2 u\right\rangle_i^k = \frac{2d}{\lambda n^0} \sum_{j \neq i} \left[\left(u_j^k - u_i^k\right)\omega(|r_j - r_i|)\right] \quad (12)$$

$$u_i^* = u_i^k + \Delta t \left(\frac{\mu}{\rho}\left\langle\nabla^2 u\right\rangle_i^k + g\right) \quad (13)$$

$$r_i^* = r_i^k + \Delta t u_i^* \quad (14)$$

Temporary particle velocities and positions are obtained. Due to the temporary movement of particles, the particle number densities may be changed; i.e. n^* deviates from n^0.

In the fourth step, pressures are explicitly calculated from temporary particle number densities n_i^* at temporary coordinates r_i^*. Based on the idea that incompressible flow is approximated as pseudo compressible, the pressures are given by the following equation of state [28,29]:

$$p_i^* = C_s^2 \rho_0 \left(\frac{n_i^* - n^0}{n^0}\right) \quad (15)$$

where C_s is the sound speed. The sound speed is chosen much larger than the velocity scales in the flow. This is generally given by the following rules [30,31]:

$$C_s^2 = \text{Max}\left(\frac{u_{max}^2}{\Delta\rho}, \frac{v_{max} u_{max}^2}{L_0 \Delta\rho}\right) \quad (16)$$

where v max is the maximum kinematic viscosity, u_{max} is the characteristics or maximum fluid velocity, L_0 is the characteristics length, and $\Delta\rho$ is the maximum allowed amount of density fluctuation. Here, $\Delta\rho$ was set 1 % to make the Mach number 0.1. This choice maintains effective incompressibility in semi-solid metal flow without making Courant condition too severe.

Then, pressure gradient term is calculated as below:

$$\langle\nabla p\rangle_i^* = \frac{2d}{n^0} \sum_{j \neq i} \frac{p_j^* + p_i^*}{2} \frac{\left(r_j^* - r_i^*\right)}{\left|r_j^* - r_i^*\right|^2} \omega(|r_j - r_i|) \quad (17)$$

$$u_i' = \Delta t\left(-\frac{1}{\rho}\langle\nabla p\rangle_i^*\right) \quad (18)$$

Finally, the particle positions and velocities are corrected:

$$u_i^{k+1} = u_i^* + u_i' \quad (19)$$

$$r_i^{k+1} = r_i^* + \Delta t u_i' \quad (20)$$

2.4 Boundary condition

The walls are represented by the STL (stereo lithography) polygons and the distance function discretization technique

is adopted from the Harada et al. [32]:

$$\langle \nabla p \rangle_{wall} = \frac{\rho}{dt^2} \frac{|dr|}{r_{iw}} r_{iw} \tag{21}$$

$$\left\langle \nabla^2 u \right\rangle_{wall} = \mu \frac{2d}{\lambda n^0} (u_{wall} - u_{particle}) Z(r_{iw}) \tag{22}$$

where μ is the friction value which is introduced as an empirical parameter. The friction value ranged 0.0–1.0 from free-slip to no-slip condition. Friction value for lower die and upper die are chosen as 0.3 and 1.0 respectively during calculation.

In the thermal calculation, the temperatures of walls are assumed to be constant. Heat transfer between walls and materials are carried according to Eq. (9) but the thermal conductivity is modified as $\zeta_j = \zeta_{wall}$. The temperature boundary condition on the free surface in SSM is modeled as convection heat transfer in Eq. (23). Free surface particles are judged by the particle number density satisfying condition $n_i^* < \beta n^0$, where β is chosen as 0.98.

$$q_n = h (T_{atm} - T_{surface}) \tag{23}$$

where h is the heat transfer coefficient (W/m^2.K), T_{atm} is atmospheric or surrounding temperature.

2.5 CFL condition

The time increments are determined using the following equations [33]:

$$\Delta t_{flow} = C_n \min \left[\frac{l_0}{|u_{max}|}, \frac{l_0^2}{v_{max}} \right] \tag{24}$$

$$\Delta t_{thermal} = \frac{C_n C_p \rho l_0^2}{k} \tag{25}$$

Here, Δt_{flow} and $\Delta t_{thermal}$ are the time increments for the flow calculation and thermal calculations. l_0 is the particle size, u_{max} is the maximum velocity, C_p is the specific heat and C_n is an empirical constant, which is given as 0.1. If Δt_{flow} is smaller than $\Delta t_{thermal}$ then a common time increment of Δt_{flow} is used to both flow and thermal calculations. As shown in the right hand side of Eq. (24) viscosity is dominant for Δt_{flow} in high viscous fluid.

2.6 Non-newtonian rheology

During the SSF process, viscosity of SSM decreases substantially as the shear rate increases; this characteristic is called pseudo plasticity. It is evident that the change of the apparent viscosity may be described by a decaying exponential function, as discussed by many researchers [34,35]. Thus, the
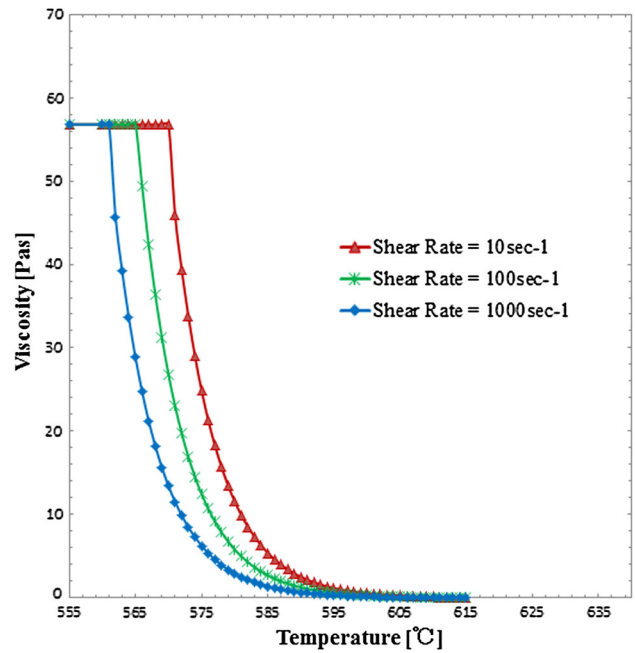

Fig. 2 Temperature viscosity relation with various shear rate considered in the non-Newtonian rheology

following power law is employed as dependency between the viscosity and the shear rate:

$$\mu_a = \mu_0 (\gamma)^m \exp(-bT) \tag{26}$$

where γ is the shear rate (sec^{-1}), m is the shear rate sensitivity, μ_0 is the viscosity coefficient (Pas), and b is the thermal sensitivity factor.

In this study SSF simulation was conducted by adopting the strain sensitivity value m of -0.3 under a shear rate ranging of $3\,\mathrm{sec}^{-1} < \gamma < 1000\,\mathrm{sec}^{-1}$. The thermal sensitivity factor b was -0.153. The graph in Fig. 2 shows the relation between viscosity and temperature with various shear rate given by Eq. (26). For numerical stability, viscosity was limited by the maximum value of 56.8 Pas. Throughout the calculation viscosity ranges as $0.01\,\mathrm{Pas} < \mu_a < 56.8\,\mathrm{Pas}$.

3 Experimental and numerical demonstrations

3.1 Flange experiment

To investigate the filling behavior and thermal distribution of various flanges, an experimental setup was conducted at Goshi Giken in Japan. The schematic diagram of die in SSF process is as shown in Fig. 3. The green color blocks were placed in between the upper die and lower die to shape the flange thickness. Four different patterns of block B were used for flange thickness of 4 , 8, 12 and 16 mm. The temperature
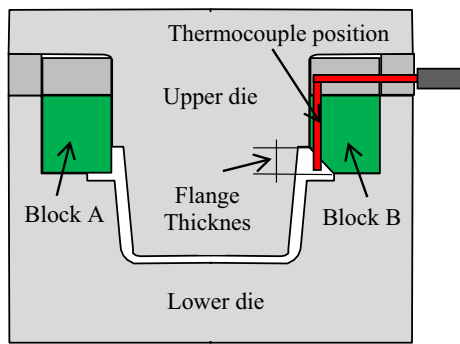
Fig. 3 Schematic diagram of the die for SSF experiment

Table 1 Experiment conditions

Experiment condition	Value	Unit
Slurry temperature	595	°C
Die temperature	150	°C
Punch velocity	100	mm/s
Slurry height	105–110	mm
Slurry radius	44–54	mm

S.N.	Isometric View	Flange Section View
Flange 4mm		
Flange 8mm		
Flange 12mm		
Flange 16mm		

Fig. 4 Result of flange experiment images

(a) Upper Die
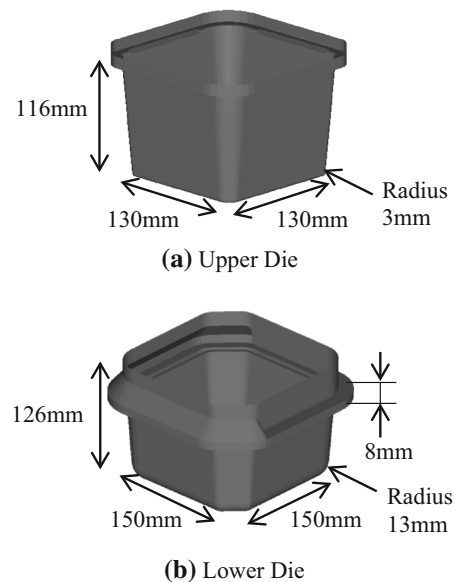
(b) Lower Die

Fig. 5 Geometry of box cavity with 16mm flange thickness. **a** Upper die, **b** lower die

sensor was placed inside the flange for the case of 16mm flange thickness only. For these experiments, semi-solid aluminum alloy AC4CH (Al-7.0 % Si-0.38 % Mg, in mass) was fabricated in the conventional furnace and stirred in a high speed rotating cylinder. The solidus and liquidus temperature of the aluminum alloy were 555 and 610 °C respectively. This slurry with 44–54 mm radius and 105 mm height for 4, 8, 12 mm flange thickness and 110 mm height for 16 mm flange thickness was pressed in a cavity shape die. The initial temperature of slurry ranged 595 °C. Similarly, the initial temperature of both upper and lower dies was 150 °C. The upper die had 100 mm/s punch velocity. Table 1 shows the summary of experimental parameters that are used as boundary conditions in simulation.

The experiments were conducted 4 times in 4 types of flange thickness (a) 4 mm (b) 8 mm (c) 12 mm and (d) 16 mm. After solidification, these flanges were cut from the center of experiment model. The flange experiment results and there section views are as shown in Fig. 4.

3.2 Analysis condition

In MPS calculation, semi-solid AC4CH aluminum slurry was represented by 109,555 particles with 2 mm particle size. Each particle has position, velocity and other physical properties. For wall boundary, three dimension STL model of box cavity with various flanges was generated using CATIA software. The geometry of dies and flanges are as shown in Figs. 5 and 6. The boundary conditions of the calculation are set sim-

ilar to the experimental conditions. Besides, to simplify the calculation, physical properties such as density, thermal conductivity, and specific heat are assumed to be constant with respect to temperature and are presented in Table 2.
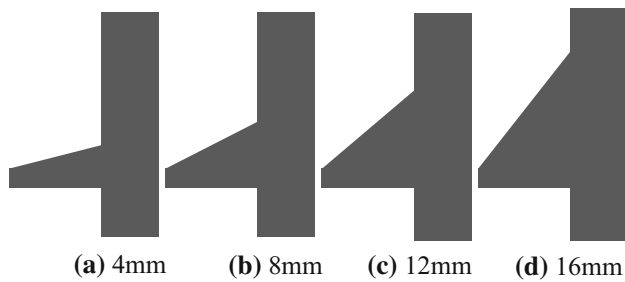
(a) 4mm **(b)** 8mm **(c)** 12mm **(d)** 16mm

Fig. 6 Pictorial images of 4 flanges **a** 4 mm, **b** 8 mm, **c** 12 mm, **d** 16 mm

Table 2 Conditions of explicit MPS analysis

Calculation condition	Value	Unit
Particle size	2	mm
Particle number	109555	–
Time increment	1.00E-5	sec
Density	2680	Kg/m^3
Thermal conductivity	159	W/mK^{-1}
Wall thermal conductivity	25	W/mK^{-1}
Specific heat	927	J/KgK^{-1}
Heat transfer coefficient	0.6	W/m^{2}K
Friction coefficient	0.3–1.0	–

3.3 Analysis results and discussion

The non-Newtonian rheological model was used to predict the flow pattern and thermal distribution in the various flanges thickness of die cavity. In the non-Newtonian rheological model the shear rate ranged $3 \sec^{-1} < \gamma < 1000 \sec^{-1}$. The apparent viscosity and temperature relation is described by Eq. (26). The initial calculation conditions were die temperature 150 °C, initial slurry temperature 595 °C, punch velocity 100 mm/s, which were the same as those of the experiments.

3.3.1 Results with flange thickness 4 mm

The filling patterns and thermal distributions of AC4CH aluminum alloy for flange thickness 4 mm are discussed in this section. As the SSM with 44–54 mm radius and 105 mm height was pressed, it takes the shape of the die as shown in Fig. 7(a–f). Similarly, Fig. 8(a–f) shows the result of temperature distributions during SSF.

The SSM solidifies faster at the top and bottom because of the long contact time with the die: the dark color represents the solidified zone. Fig 9(a–c) shows that the SSM flows straight upward and flange cavity is filled later. The temperature distribution of SSM near the wall around flange is solidified faster than the mid area of the flange.
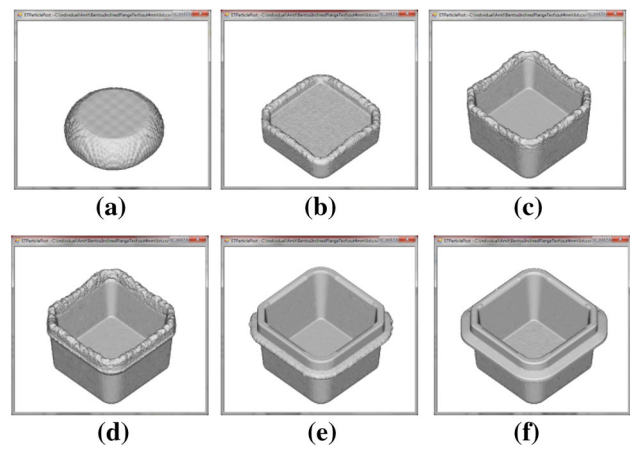
(a) **(b)** **(c)**

(d) **(e)** **(f)**

Fig. 7 Filling pattern with flange thickness 4mm: **a** $t = 0.504$ s, **b** $t = 0.672$ s, **c** $t = 0.8$ s, **d** $t = 0.856$ s, **e** $t = 0.9$ s, **f** $t = 0.936$ s

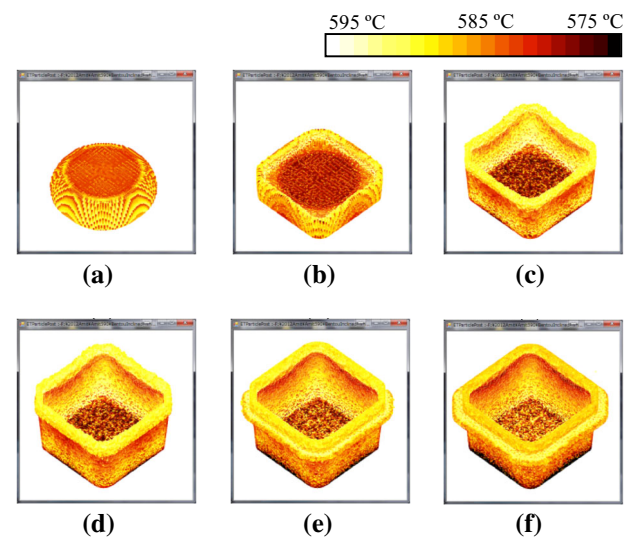

595 ºC 585 ºC 575 ºC

(a) **(b)** **(c)**

(d) **(e)** **(f)**

Fig. 8 Temperature contour with flange thickness 4mm: **a** $t = 0.504$ s, **b** $t = 0.672$ s, **c** $t = 0.8$ s, **d** $t = 0.856$ s, **e** $t = 0.9$ s, **f** $t = 0.936$ s
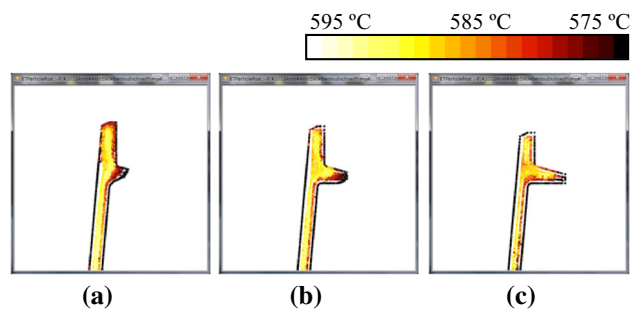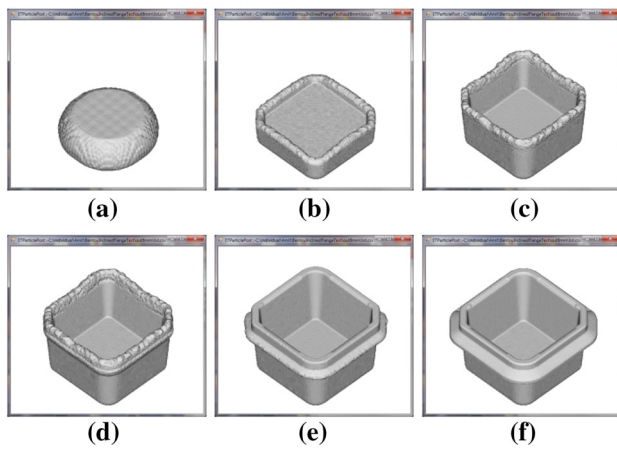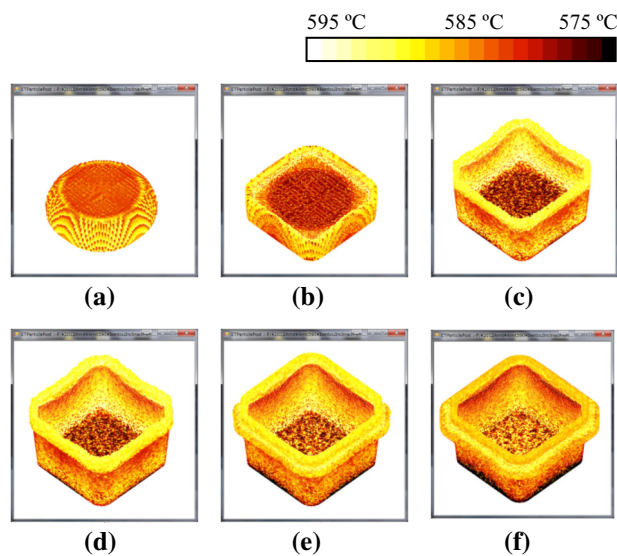

595 ºC 585 ºC 575 ºC

(a) **(b)** **(c)**

Fig. 9 Temperature contour around flange at thickness 4 mm: **a** $t = 0.888$ s, **b** $t = 0.904$ s, **c** $t = 0.936$ s

3.3.2 Results with flange thickness 8 mm

Figure 10(a–f) shows the filling patterns of AC4CH aluminum alloy for flange thickness 8 mm.

Fig. 10 Filling pattern with flange thickness 8 mm: **a** $t = 0.504$ s, **b** $t = 0.672$ s, **c** $t = 0.8$ s, **d** $t = 0.856$ s, **e** $t = 0.9$ s, **f** $t = 0.936$ s

Fig. 11 Temperature contour with flange thickness 8 mm: **a** $t = 0.504$ s, **b** $t = 0.672$ s, **c** $t = 0.8$ s, **d** $t = 0.856$ s, **e** $t = 0.9$ s, **f** $t = 0.936$ s

The temperature distributions of SSM during SSF are shown in Fig. 11(a–f). The temperature at the top and bottom of SSM have lowest temperature at $T = 578\,°C$ due to conduction heat transfer with the die. Figure 12(a–c) shows the filling pattern and temperature contour of SSM around 8 mm flange. The SSM has a higher temperature in the mid area of the flange at $T = 588\,°C$ than temperature near the wall at $T = 578\,°C$.

3.3.3 Results with flange thickness 12 mm

For 12 mm flange thickness, the filling patterns of AC4CH aluminum alloy are shown in Fig. 13(a–f). As the SSM with 44–54 mm radius and 105 mm height was pressed by the
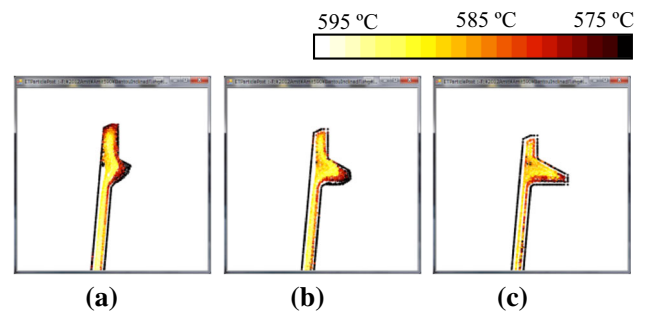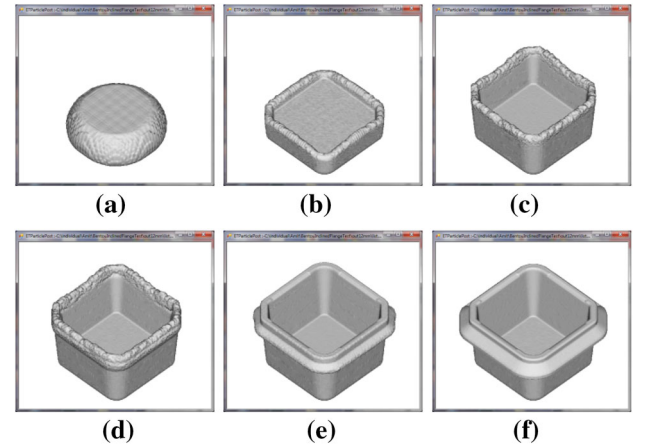

Fig. 12 Temperature contour around flange at thickness 8 mm: **a** $t = 0.888$ s, **b** $t = 0.904$ s, **c** $t = 0.936$ s

Fig. 13 Filling pattern with flange thickness 12 mm: **a** $t = 0.504$ s, **b** $t = 0.672$ s, **c** $t = 0.8$ s, **d** $t = 0.856$ s, **e** $t = 0.9$ s, **f** $t = 0.936$ s
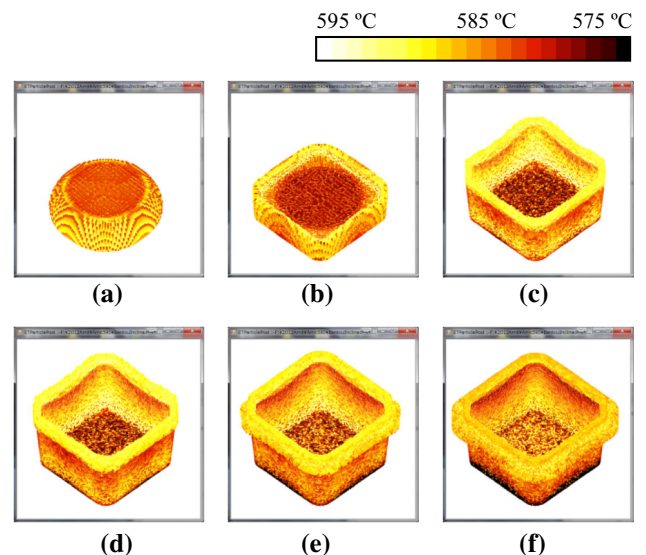

Fig. 14 Temperature contour with flange thickness 12 mm: **a** $t = 0.504$ s, **b** $t = 0.672$ s, **c** $t = 0.8$ s, **d** $t = 0.856$ s, **e** $t = 0.9$ s, **f** $t = 0.936$ s

velocity of 100 mm/s, it flows from lower cavity to the upper cavity and then flange is filled simultaneously.

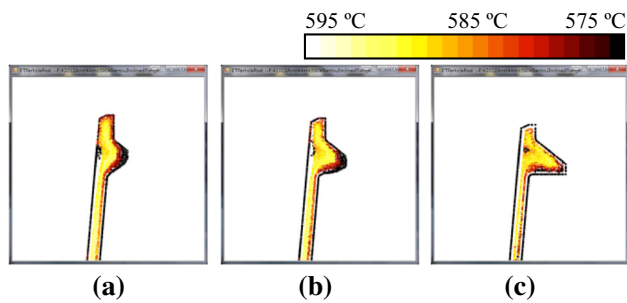As shown in Fig. 14(a–f) the top and bottom of SSM have the lowest temperature at $T = 578\,°C$ due to conduction

Fig. 15 Temperature contour around flange at thickness 12 mm: **a** $t = 0.888$ s, **b** $t = 0.904$ s, **c** $t = 0.936$ s
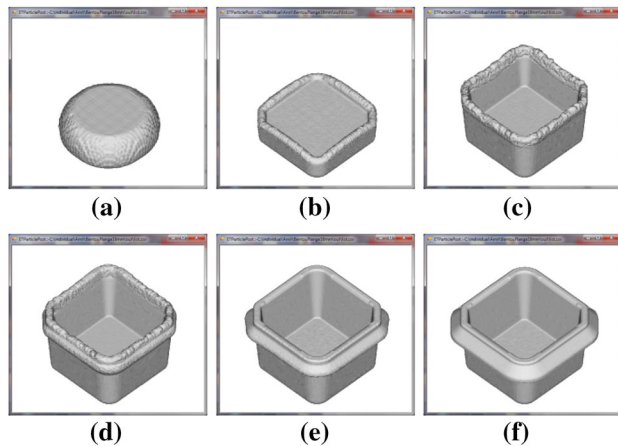

Fig. 16 Filling pattern with flange thickness 16 mm: **a** $t = 0.56$ s, **b** $t = 0.736$ s, **c** $t = 0.896$ s, **d** $t = 0.96$ s, **e** $t = 0.992$ s, **f** $t = 1.032$ s

Fig. 17 Temperature contour with flange thickness 16 mm: **a** $t = 0.56$ s, **b** $t = 0.736$ s, **c** $t = 0.896$ s, **d** $t = 0.96$ s, **e** $t = 0.992$ s, **f** $t = 1.032$ s

Fig. 18 Temperature contour around flange at thickness 12 mm: **a** $t = 0.984$ s, **b** $t = 1.0$ s, **c** $t = 1.032$ s

heat transfer with the die. The temperature distributions of SSM around 12mm flange are shown in Fig. 15(a–c). The SSM has a higher temperature in the mid area of the flange at $T = 588\,°C$ than temperature near the wall at $T = 578\,°C$. This result is similar to the flange thickness 8 mm. But as the flange thickness increases from 8 to 12 mm the solidification region or zone also increases in the mid area of the flange as shown in Figs. 12c and 15c.

3.3.4 Results with flange thickness 16 mm

For 16 mm flange thickness, the SSM with radius 44–54 mm and height 110 mm was punched by 100 mm/s velocity. The filling patterns of AC4CH aluminum alloy are as shown in Fig. 16(a–f).

The temperature distributions for flange thickness 16mm are as shown in Fig. 17(a–f). The temperatures at top and bottom of SSM have lowest temperature at $T = 577\,°C$. This is 1C lower than the previous cases with flange thickness 8 and 12 mm, it's because the initial height of the SSM is previous case was 105 mm and press time was 0.936 s but in this case, with flange thickness 16 mm the initial height of the SSM material is 110 mm and press time 1.036 s. Thus it has longer contact time with the upper and lower die. The
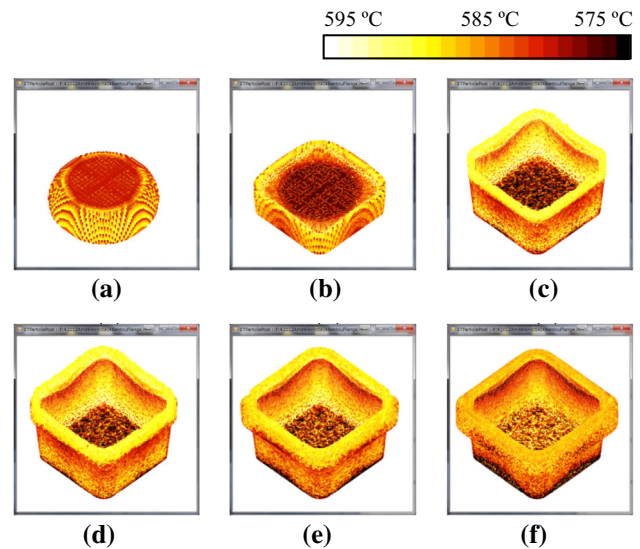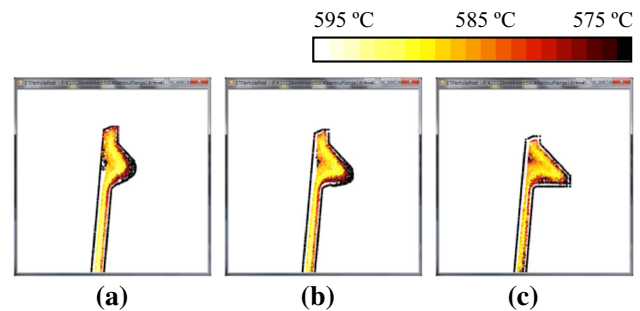
temperature distributions of SSM around 16mm flange are shown in Fig. 18(a–c). The SSM have higher temperature in the mid area of the flange at $T = 588\,°C$ than temperature near the wall at $T = 577\,°C$. As the flange thickness increases from 4, 8, 12 and 16 mm the hot SSM material flowing in the flange is higher. The mid area of flange is hotter and bright and it takes much time to solidify as shown in Fig. 18c.

3.3.5 Solidification and validation

After complete filling simulation with the non-Newtonian rheological model, solidification computation was performed in the experiment model with flange thickness 16 mm. The schematic diagram of solidification phenomena during experiment was as shown in Fig. 2. During solidification experiment, the temperature of upper and lower die was recorded at $T_{die} = 250\,°C$ and green block $T_B = 200\,°C$. The temperature data of the SSM was collected with the help of thermocouple positioned inside the flange. During the solidification simulation, thermal conductivity was set

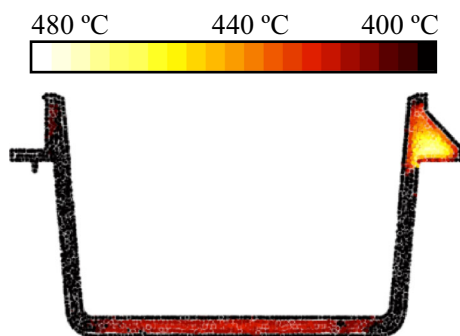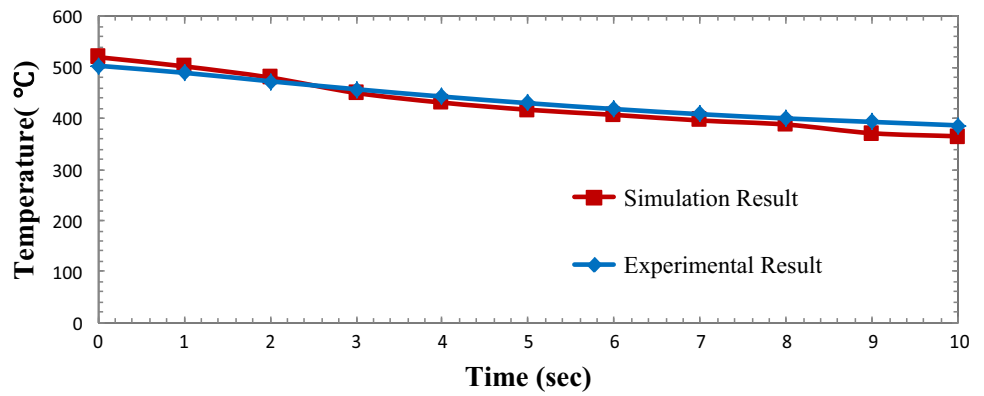**Fig. 19** History curve of temperature during solidification

Fig. 20 Temperature distribution at 3 s (flange thickness 16 mm)
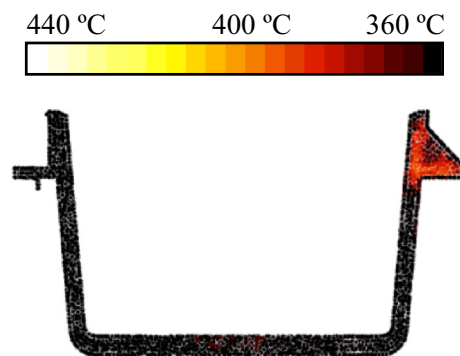

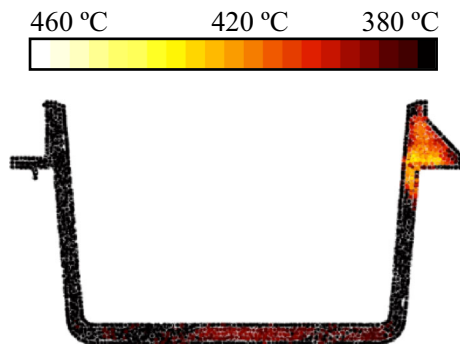**Fig. 22** Temperature distribution at 9 s (flange thickness 16 mm)

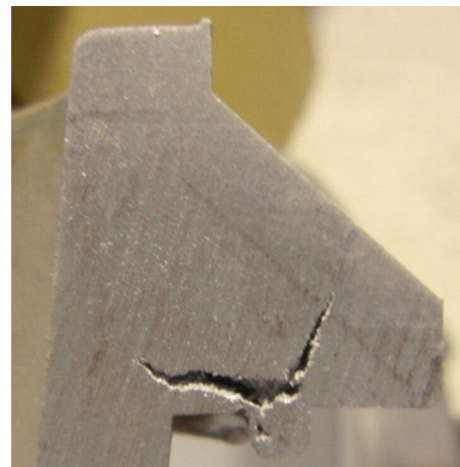**Fig. 21** Temperature distribution at 6 s (flange thickness 16 mm)

Fig. 23 Shrinkage defect in flange thickness 16 mm during solidification experiment

as 180 W/m.K^{-1} and other parameters like density, specific heat capacity, density, and wall thermal conductivity were kept constant as shown in Table 2.

Figure 19 is the history curve of temperature measured in solidification analysis and experiment recorded for 10 s. Figs. 20, 21 and 22 are the temperature distributions at time 3, 6 and 9 s, respectively. The temperature around the flange at 3, 6 and 9 s are found to be $T = 450\,°C$, $T = 407\,°C$ and $T = 371\,°C$, respectively. This shows that, as the time increases the solidification of SSM starts near from the wall towards the mid area of the flange this is because of heat conduction from the wall.

Figure 23 shows the shrinkage defect near flange with 16 mm thickness during solidification experiment. The temperature distribution in Fig. 22 also shows the higher temperature zone near the lower mid area of the flange. This temperature distribution during solidification provides the good prediction of shrinkage location near the flange.

3.4 Conclusions

In this paper, the flow and thermal simulation of AC4CH aluminum alloy was simulated in box cavity with various

flange thickness using the explicit MPS method. The non-Newtonian rheological model was used to simulate the flow characteristics. The filling patterns and thermal distributions of SSM for various flange thickness were simulated. As the flange thickness increases from 4, 8, 12 and 16 mm the solidification region in the mid area of the flange also increases. After complete filling simulation, solidification simulation was conducted in 16 mm thickness flange cavity. Temperature decrease in the flange was validated with the experimental data and the shrinkage defect was well predicted near the lower mid area of the flange.

Die design is very important step while practicing forging process with semi-solid material. Thus, the explicit MPS method used in this study can be helpful to predict the influence among the die design, filling pattern and solidification phenomena of semi-solid material.

References

1. Kapranos P, Ward PJ, Atkinson HV, Kirkwood DH (2000) Near net shaping by semi-solid metal processing. Mater Des 21:387–394
2. Omar MZ, Atkinson HV, Kapranos P (2011) Thixotropy in semi-solid steel slurries under rapid compression. Metall Mater Trans A 42:2807–2819
3. Miller WS, Zhuang l, Bottema J, Wittebrood AJ, Smet PD, Haszler A, Vieregge A (2000) Recent development in aluminum alloys for the automotive industry. Mater Sci Eng A 280:37–49
4. Atkinson HV (2010) Semisolid processing of metallic materials. Mater Sci Technol 26:1401–1413
5. Chou HN, Govender G, Ivanchev L (2006) Opportunities and challenges for use of SSM forming in the aerospace industry. Solid State Phenom 116–117:92–95
6. Salleh MS, Omar MZ, Syarif J, Mohammed MN (2013) An overview of semisolid processing of aluminium alloys. ISRN Mater Sci 2013:1
7. Kirkwood DH (1994) Semi solid metal processing. Int Mater Rev 39:103–117
8. Spencer DB, Mehrabian R, Flemings MC (1972) Rheological behaviour of Sn-15 Pct Pb in the crystallization range. Metall Trans A 3:1925–1932
9. Kiuchi M, Yanagimoto J, Sugiyama S (1998) Mashy metal/alloy joining a new process for manufacturing new products. Ann CIRP 47:227–230
10. Kiuchi M, Yanagimoto J, Yokobayashi H (2001) Flow stress yield criterion and constitutive equation of mushi/semi-solid alloy. Ann CIRP 50:157–160
11. Nishi NN, Egoshi Y, Takahashi Y (1986) Solidified structure of squeeze casting. Jpn Die Cast Assoc JD86–16:154–163
12. Iwahori H, Tozawa K, Yamamoto Y, Nakamura M (1984) Formation of scattered structures in aluminum alloy die castings. J Jpn Inst Light Met 34:389
13. Nishi NN, Komazaki T, Takahashi Y (1991) Formation mechanism of aluminum die castings microstructures. Jpn Foundrym Soc 63:347
14. Moritaka M, Fujisawa S, Andou Y (1998) The effect of the billet microstructure on formability and product quality in the mushy-state forming of Al-Si-Mg alloy. J Jpn Soc Technol Plast 39:28–32
15. Cho WG, Kang CG (2000) Mechanical properties and their microstructure evaluation in the thixoforming process of semi-solid aluminum alloys. J Mater Process Technol 105:269–277
16. Kitamura K, Ando Y, Hironaka K, Yahata S, Yoshida C (1997) Die casting of aluminum alloy in semi-solid state. In: Proceedings of the third international conference on semi-solid processing of alloys and composites, pp 181–190. The University of Tokyo, Tokyo
17. Phillion AB, Cockcroft SL, Lee PD (2008) A new methodology for measurement of semi-solid constitutive behavior and its application to examination of as-cast porosity and hot tearing in aluminum alloys. J Mater Sci Eng A 491:237–247
18. Choi SW, Kim G, Bae J, Kim YD (2009) Ultrasonic treatment for fragmentation at solidification of aluminum alloy. In: ICROS-SICE international joint conference. Fukuoka international congress center, pp 378–382
19. Charreyron PO, Flemings MC (1985) Rheology of semi-solid dendritic Sn–Pb alloys at low strain rates. Int J Mech Sci 27:781–791
20. Nguyen TG, Favier D, Suery M (1994) Theoretical and experimental study of the isothermal mechanical behavior of alloys in the semi-solid state. Int J Plast 10:663–693
21. Kang CG, Choi JS, Kang DW (1998) A filling analysis of the forging process of semi-solid aluminum materials considering solidification phenomena. J Mater Process Technol 73:289–302
22. Lee DH, Seo PK, Kang CG (2004) Die design by filling analysis of semi-solid injection forging process and their experimental investigation. J Mater Process Technol 147:45–50
23. Cleary PW, Ha J, Prakash M, Nguyen T (2006) 3D SPH flow predictions and validation for high pressure die casting of automotive components. Appl Math Model 30:1406–1427
24. Cleary PW, Ha J (2002) Three-dimensional smoothed particle hydrodynamics simulation of high pressure die casting of light metal components. J Light Met 2:169–183
25. Cleary PW, Savage G, Ha J, Prakash M (2014) Flow analysis and validation of numerical modelling for a thin walled high pressure die casting using SPH. Comput Part Mech 1:229–243
26. Koshizuka S, Tamako H, Oka Y (1995) A particle method for incompressible viscous flow with fluid fragmentation. Comput Fluid Dyn J 4:29–46
27. Hirata N, Anzai K (2011) Numerical simulation of shrinkage formation of pure Sn casting using particle method. Mater Trans 52:1931–1938
28. Oochi M, Koshizuka S, Sakai M (2010) Explicit MPS algorithm for free surface flow analysis. Trans JSCES, paper no. 20100013
29. Oochi M, Yamada Y, Koshizuka S, Sakai M (2011) Validation of pressure calculation in explicit MPS method. Trans JSCES, paper no 20110002
30. Fang HS, Bao K, Wei JA, Zhang H, Wu EH, Zheng L (2009) Simulation of droplet spreading and solidification using an improved SPH model. Numer Heat Trans Part A 55:124–143
31. Cleary PW, Ha J, Prakash M, Nguyen T (2006) 3D SPH flow predictions and validation for high pressure die casting of automotive components. Appl Math Model 30:1406–1427
32. Harada T, Koshizuka S, Shimazaki K (2008) Improvement of wall boundary calculation model for MPS method. Trans JSCES, paper no 20080006
33. Cleary PW, Ha J (2006) Modelling confined multi-material heat and mass flow using SPH. Appl Math Model 22(12):981–993
34. Kirkwood DH, Ward PJ (2004) Modeling of thixotropic breakdown. In: Proceedings of the 8th international conference on the processing of semi-solid alloys and composite, pp 9–13. Limassol
35. Quaak CJ, Katgerman L, Kool WH (1996) Viscosity evolution of partially solidified aluminum slurries after a shear rate jump. In: Proceedings of the 4th international conference on the processing of semi-solid alloys and composite, pp 35–39. Sheffield